

Astrocytic Ion Dynamics: Implications for Potassium Buffering and Liquid Flow

Geir Halmes^{1,*}, Klas H. Pettersen², Leiv Øyehaug³, Marie E. Rognes^{4,5}, Hans Petter Langtangen⁴, Gaute T. Einevoll^{1,6}

1 Dept. of Mathematical Sciences and Technology, Norwegian University of Life Sciences, Ås, Norway

2 Letten Centre and GliaLab, Centre for Molecular Medicine, University of Oslo, Oslo, Norway

3 Dept. of Computer Science, Oslo and Akershus University College of Applied Sciences, Oslo, Norway

4 Simula Research Laboratory, Fornebu, Norway

5 Dept. of Mathematics, University of Oslo, Oslo, Norway

6 Dept. of Physics, University of Oslo, Oslo, Norway

*** E-mail: geir.halmes@nmbu.no**

Abstract

We review modeling of astrocyte ion dynamics with a specific focus on the implications of so-called spatial potassium buffering where excess potassium in the extracellular space (ECS) is transported away to prevent pathological neural spiking. The recently introduced Kirchhoff-Nernst-Planck (KNP) scheme for modeling ion dynamics in astrocytes (and brain tissue in general) is outlined and used to study such spatial buffering. We next describe how the ion dynamics of astrocytes may regulate microscopic liquid flow by osmotic effects and how such microscopic flow can be linked to whole-brain macroscopic flow. We thus include the key elements in a putative multiscale theory with astrocytes linking neural activity on a microscopic scale to macroscopic fluid flow.

1 Introduction

Brain function is fundamentally about movement of ions and molecules. When modelling neuronal dynamics, it is common to neglect the dynamics of individual ion species, and rather just simulate the net electrical currents and resulting changes in membrane potentials. The justification is that on the typical time scale of neural integration (milliseconds), the concentrations of the major charge carriers in brain tissue (i.e., Na^+ , K^+ , Cl^- , ...) vary little. For astrocytic dynamics the situation is different. For one, the typical time scale for astrocytic membrane processes are longer, i.e., seconds rather than milliseconds, so that the fixed ion-concentration assumption is *a priori* more dubious. Further, many key astrocytic functions are related just to their responses to shifts in extracellular ion concentrations [1].

Astrocytes have several homeostatic functions in the brain. They provide metabolic support for neurons, synthesize extracellular matrix proteins, adhesion molecules, and trophic factors controlling neuronal maturation, are involved in the formation of blood vessels and in maintenance of the blood-brain barrier, and maintain the ECS via uptake of K^+ and neurotransmitters [1]. Here, we describe theoretical frameworks for modelling astrocytic ion concentration

dynamics, with particular focus on K^+ clearance mechanisms, and possible consequences for microscopic liquid flow in the brain.

When neurons fire action potentials (APs), they absorb Na^+ and expel K^+ from/to the ECS. At low to moderate firing frequencies, the time interval between two APs is sufficient for neuronal Na^+-K^+ pumps to restore the baseline levels of Na^+ and K^+ . Ion concentrations then remain essentially constant over time [2]. However, during periods of intense neural signalling, the neuronal ion pumps may fail to keep up, and ECS ion concentrations can change significantly [3–8]. The most critical effects of this relates to changes in the K^+ -concentration in the ECS, which can increase from a relatively low baseline level of around 3 mM up to levels between 8 and 12 mM during non-pathological conditions [7, 9, 10]. Increases beyond this can occur under pathological conditions such as hypoxia, anoxia, ischemia epilepsy and spreading depression [11–14]. During spreading depression, K^+ -concentrations in the ECS can become as high as 60 mM [15].

Astrocytes have several membrane mechanisms for local uptake of excess K^+ [1, 2, 6, 7, 10, 16–18]. They are therefore likely to play a role in pathological conditions related to ion dynamics in the ECS, and evidence suggest that changes in astrocytic function is implicated in spreading depression, epilepsy and ischemia [19, 20]. In Section 2 we briefly review some modelling works that have investigated the relationship between astrocytic regulation of ECS K^+ and neuronal firing patterns.

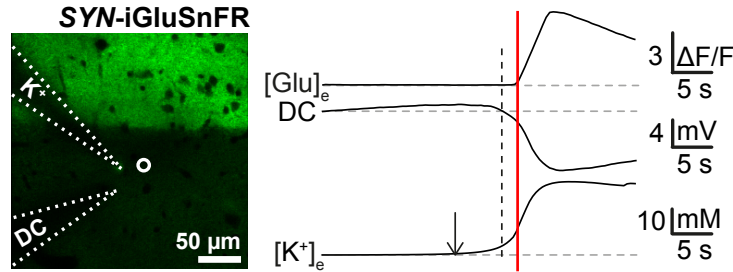


Figure 1. Changes in extracellular K^+ concentration, extracellular glutamate and extracellular potential (DC) during cortical spreading depression. *Left:* The green fluorescent tracer shows the extracellular glutamate wave, which travels with a speed of 50 $\mu m/s$. The dashed white lines indicate the positioning of the recording electrodes, while the solid white line shows the region of interest (ROI) for glutamate. *Right:* The glutamate signal within the ROI ($[Glu^+]_e$, upper), extracellular potential (DC, middle) and extracellular K^+ concentration ($[K^+]_e$, lower), all as functions of time. The figure is modified from Fig. 4 in Enger et al. [12].

Increases in the ECS K^+ -concentration are often accompanied by a slow negative shift in the ECS potential. These potential shifts can be on the order of a few millivolts [4, 5, 11, 21, 22]. Figure 1 shows an extreme example from an experiment on cortical spreading depression, where a K^+ -concentration shift of 20-30 mM was accompanied by a 5-10 mV shift in the ECS potential [12]. It has been argued that this link between sustained potentials and the ECS K^+ concentration is the signature of glial K^+ buffering currents [5]. In addition to local uptake and storage in astrocytes [5, 23], clearance of excess K^+ from local high-concentration regions

may occur by transport through the ECS [24], and by a process coined *spatial K^+ buffering*, where astrocytes take up K^+ from high concentration regions, transport it intracellularly, and release it in regions where the ECS concentration is lower [6, 7, 10, 16, 25]. As astrocytes often are interconnected by gap junctions into a syncytium, intracellular transport can in principle occur over quite large distances and via several cells [7]. The relative importance of these different clearance mechanisms are under debate [26]. As these processes involves variations in both ionic concentrations and electrical potentials, ionic transports may be propelled both by voltage- and concentration gradients [27]. In Section 3, we explore spatial K^+ buffering in detail, and present a recently developed biophysical modelling formalism for simulating electrodiffusive processes - the *Kirchhoff-Nernst-Planck (KNP)* scheme.

Changes in ionic concentrations will also induce osmotic pressures, which may lead to water uptake, astrocyte swelling and micropscopic liquid flow in the brain [18, 28]. A complete modelling framework that combines spatial K^+ buffering processes with processes related to water flows is currently lacking, but in Section 4.2, we review the theoretical foundation that such a framework would need to be based on.

2 Influence of glial K^+ buffering on neuronal activity

The effect of ion-concentration shifts on neuronal activity can to a large extent be explained by its impact on the reversal potential e_k of an ion species k :

$$e_k = \frac{\psi}{z_k} \log([k]_E/[k]_I). \quad (1)$$

As Eq. 1 shows, the reversal potential depends on the ion concentrations on the outside ($[k]_E$) and inside ($[k]_I$) of the membrane (z_k is the valence of ion species k , and $\psi = RT/F$ where R is the gas constant, T the absolute temperature, and F is Faraday's constant). For example, when K^+ accumulates in the ECS, the K^+ reversal potential will increase. As a consequence, neurons will become depolarized and brought closer to their firing threshold, which in turn may lead to enhanced neuronal activity and to further increases in $[K^+]_e$. Computational models that study disorders related to extracellular K^+ are many (see e.g., [13, 14, 18, 29–35]). Figure 2 shows an example from a previous modelling study where we explored the positive feedback loop described above [18]. The model used in [18] combined a Hodgkin-Huxley type neuron model [31] with a detailed model of glial membrane ion and water transport [28].

Figs. 2A,B show the results of two numerical simulations of the neuron-glia model when the neuron was stimulated by electrical currents of different durations and magnitudes. Elevated levels of $[K^+]_E$ were observed both with the briefest current stimulation (Fig. 2A) and a longer and stronger current stimulation (Fig. 2B). However, in terms of the resulting spiking patterns, the difference was striking: with the briefest stimulation, the neuron fired several APs after the stimulation had ceased, and then returned to the resting state. By contrast, the larger and longer stimulus drove the neuron into a deactivated state where the neuron lingered at a depolarized level with a non-zero K^+ -efflux. In this case, $[K^+]_E$ reached very high levels (Fig. 2B, inset). The behaviour encountered in the former situation is referred to as *spontaneous discharge*, while the latter situation is referred to as *depolarization block*.

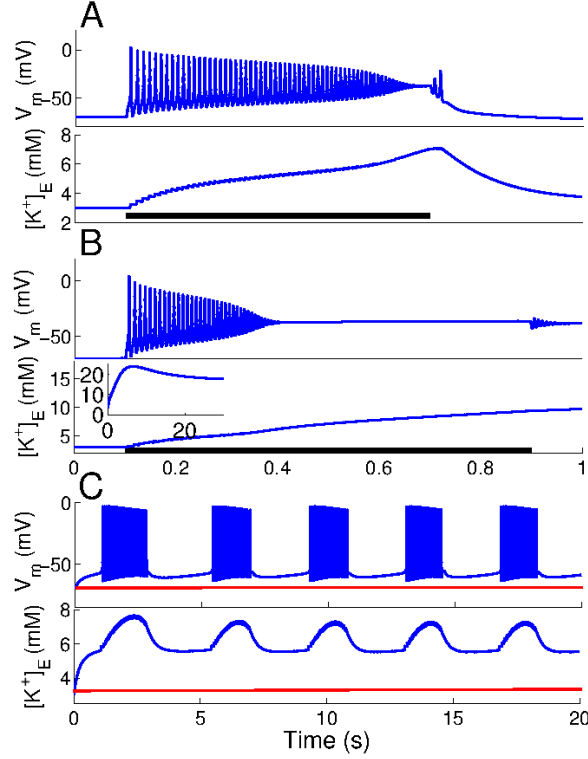


Figure 2. Dynamical repertoire of neuron-glia model. The model [18] included voltage-gated sodium and potassium channels and the NaKATPase pump in the neuronal membrane (following Kager et al. [31]), and sodium, potassium and chloride channels, as well as the NaKATPase pump, the NKCC1 and NBC cotransporters and water channels in the glial membrane [28]. To ensure charge neutrality of the ECS, the assumption was made that the amounts of sodium and potassium crossing the neuronal membrane were identical so that the cation current was exactly zero. A, B: Dynamics of neuronal membrane potential V_m (top) and $[K^+]_E$ (bottom) when the neuron was stimulated (A) with a short pulse of relatively small magnitude, and (B) with a longer pulse of larger magnitude (inset in (B) shows long-time dynamics). C: Dynamics of neuronal membrane potential V_m (top) and $[K^+]_E$ (bottom) compared to resting conditions (red lines) in absence of stimulation with a reduction of the maximum rate of the glial sodium-potassium pump by a factor 0.62, see [18] for details.

Whereas Figs. 2A and B illustrate the interplay between neuronal activity and $[K^+]_E$, Fig. 2C shows more directly the effect that astrocytes may have on neurodynamics. Here, the neuron received no external input. When the astrocyte had the default parametrization, $[K^+]_E$ was maintained at a low level, and the neuron was at rest (red lines). However, when we modelled astrocytic dysfunction as a reduction in the astrocyte's Na^+/K^+ -pump rate, $[K^+]_E$ increased, and drove the neuron into periodic bursting. This bursting behaviour, also encountered in another model of neuron-glia interaction [33], was previously observed in experiments and has been interpreted as relevant to some types of epilepsy [36, 37]. Further, in human epilepsy patients it has been found that the overall activity of NaKATPase is reduced [38], consistent with the results in Fig. 2, showing that neurons are more likely to fire spontaneous discharges, go into depolarization block or display bursting behaviour when the glial sodium-potassium pump rate was reduced.

Fig. 2 just showed a few illustrative examples on how K^+ buffering can be relevant for neurodynamics. For a more thorough analysis of this, we refer to the original publication [18], where we presented a bifurcation analysis that systematically mapped out how different neuronal firing states depended on variations in selected model parameters. In the following, we direct our focus towards the glial K^+ buffering process as such.

3 An electrodiffusive model of spatial K^+ buffering by astrocytes

Unlike neurons, glial cells are not predominantly driven by synaptic input, and do not produce fast unitary events such as action potentials. To a large extent, astrocytic membrane dynamics appears rather to be driven by slow variations in ECS ion concentrations and voltage differences between the ECS and the intracellular astrocytic space. Astrocyte resting membrane potentials have been reported to be heterogeneous, in part because of the heterogeneity in K^+ conductance [39, 40]. However, as a tentative approximation, we assume that all astrocytes within a (relatively large) spatial region receive roughly the same input and perform roughly the same processing, and can be collapsed into a single astrocyte domain, representing the mass average astrocytic response (this assumption was motivated previously [6, 7, 25]). Furthermore, astrocytes are often coupled with gap junctions, allowing intracellular ionic transports over larger distances through a syncytium of many interconnected cells [7, 12]. Intracellular transports in the astrocyte domain are therefore conceptually similar to ECS transports, and not limited by the spatial extension of a single cell.

A framework for modelling long term astrocytic processing on an extended spatial scale is summarized in Fig. 3. As argued above, transport processes through the ECS and the astrocytic syncytium (panel A) can be described by a simplified two domain model (panel B), which includes an ECS domain and an astrocyte domain that exchange ions via typical astrocytic membrane mechanisms. In this aspect, the astrocyte modelling framework is simpler than computational neural models, which are often described with a high degree of spatial specificity. However, in the spatial K^+ buffering model, axial fluxes in the ECS or inside the astrocyte must be described by the Nernst-Planck equations for electrodiffusion (see Section 3.1). Then not only electrical currents, but also ion concentration dynamics are explicitly modelled. In this

aspect, the astrocyte modelling framework is more complex than computational neural models.

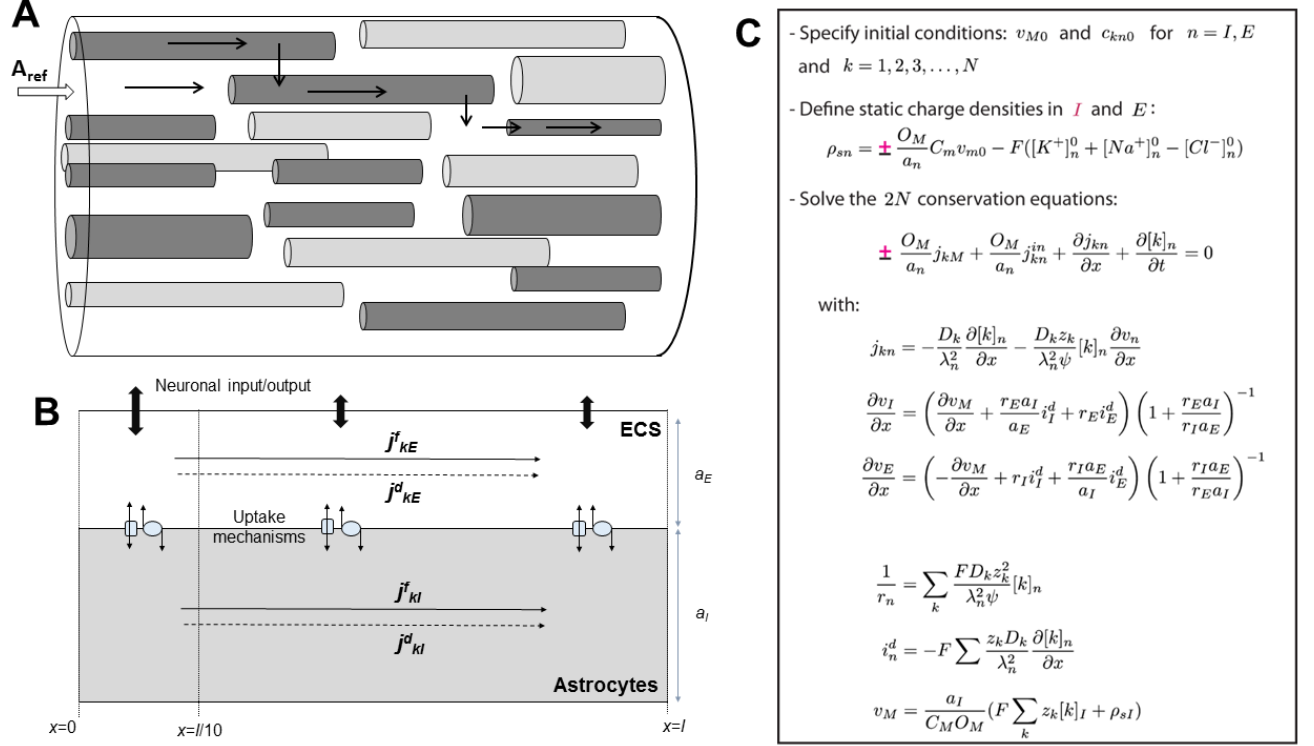


Figure 3. A two domain-model for ion concentration dynamics in astrocytes and extracellular space when macroscopic transport is essentially one-dimensional. (A) A piece of brain tissue with cross section area A_{ref} and an arbitrary extension l in the x -direction. Tissue astrocytes (dark grey) participate in the transport process, other cells do not (light grey). (B) The interior of all astrocytes represented as a single domain (essentially an equivalent cylindrical cable coated by ECS), where all parts of all astrocytes at a given location x are assumed to undergo the same activity. Here, a_I and a_E are, respectively, the fractions of A_{ref} occupied by astrocytes and the ECS. Due to the presence of other cells (non-participatory), we generally have that $a_I + a_E < 1$. The astrocyte domain exchanges ions with the ECS via astrocytic membrane mechanisms. Axial transport processes in the ECS and inside astrocytes occur due to electrical migration (j^f) and diffusion (j^d). Neuronal activity is represented as an external input to the ECS. Enhanced neuronal input to a specific region of the ECS (e.g., the region $0 < x < l/10$ in the figure) will evoke spatial buffering processes in the system. (C) A set of equations that summarizes the electrodiffusive formalism. In equations containing the symbol " \pm ", " $+$ " should be used for intracellular domain ($n = I$) and " $-$ " should be used for the extracellular domain ($n = E$). The formalism is general to the choice of j_{kM} , representing system specific membrane mechanisms (ion pumps, ion channels, cotransporters ect.), which will depend on the case at hand. External input to the system must also be specified. The figure was modified from [25].

3.1 Model constituents

In computational neuroscience the main focus has been on modelling the short-term electrical signalling of neurons. Integration of synaptic input and generation of action potentials typically take place on a time scale of less than 100 milliseconds. At this short time-scale, ionic concentrations of the main ionic charge carriers (Na^+ , K^+ and Cl^-) vary little. With the possible exception of the signalling molecule Ca^{2+} (see e.g., [41, 42]), ion concentrations are typically assumed to be constant during the simulated period or, at least, to vary so little that they do not evoke notable diffusive currents. This is, for example, an underlying assumption in the cable equation (e.g. [43, 44]), upon which most multicompartamental neural models are built.

Contrarily, spatial K^+ buffering by astrocytes typically takes place at the time scale of seconds, and must account for ion concentration changes. The dynamics of ion concentrations will not only depend on transmembrane fluxes, but also on intra- and extracellular transports due to diffusion (along concentration gradients) and electrical migration (along voltage gradients) [7, 25, 27]. If ion concentration gradients become sufficiently steep, the electrical currents associated with diffusion of charged ions can be of comparable magnitude to the Ohmic currents driven by electrical fields, and will therefore influence the electrodynamics of the system [25, 45]. An accurate description of long time scale processing in brain tissue thus calls for an electrodiffusive formalism based on the Nernst-Planck equations.

In earlier, pioneering modelling works on astrocytic K^+ -buffering [6, 7, 10, 46], the transient charge accumulation associated with the capacitive membrane current was neglected. Due to this, the models might be inaccurate in responses to transient signals, and do not guarantee a strictly consistent relationship between electrical fields and ionic concentrations. Given that K^+ -buffering likely depends on an intricate balance between diffusive and field-driven forces, this short-coming inspired us to develop a new model [25], which we present below. A key achievement of that work was the derivation of the general mathematical equations for electrodiffusion in a two domain setup as that in Fig. 3B.

3.1.1 Kirchhoff-Nernst-Planck framework

The challenge in solving the Nernst-Planck equations typically lies in how to compute the local electrical potential v . Generally, v can be computed from Poisson’s equations, as it is done in Poisson-Nernst-Planck solvers [47–51]. However, to do this one must explicitly model charge relaxation processes, which demands an extremely fine spatiotemporal resolution [52]. This makes Poisson-Nernst-Planck solvers computationally expensive and unsuited for predictions at a tissue level. For the K^+ -buffering model [25], we developed an alternative framework, which we may refer to as the Kirchhoff-Nernst-Planck (KNP) framework. The KNP-framework is summarized in Fig. 3C, and briefly introduced below. Useful entities and parameter definitions are listed in Table 1. For a full derivation of this formalism, the reader is referred to the original work [25].

The KNP-framework is a means of solving the continuity equations for the one-dimensional model system in Fig. 3B, for the intracellular ($n = I$) and ECS ($n = E$) domains, for all ion species k with valence z_k and concentration $[k]_n$. The longitudinal intra- and extracellular fluxes are described by the Nernst-Planck equation, i.e., j_{kn} in Fig. 3C, where first term on the right

represents the diffusive flux density (j_{kn}^d), and the last term is the flux density due to ionic migration in the electrical field (j_{kn}^f).

Instead of using Poisson's equation to derive v , the KNP-framework derives the voltage gradients ($\partial v / \partial x$ in Fig. 3C) from the constraint that the sum of currents into a compartment should always be zero (i.e., Kirchhoff's current law). This zero-sum includes longitudinal diffusive- and field currents, transmembrane ionic currents and transmembrane capacitive currents. The three first of these are ionic currents, whereas the latter reflects the accumulation of charge on the astrocyte membrane. Hence, in the KNP-framework, the total electrical charge in a compartment is always consistent with the membrane charge associated with the membrane potential v_M , whereas the bulk solution is always electroneutral [25]. This is typically true for the bulk solution in brain tissue at time scales larger than 1 nanosecond [53].

The KNP-framework has proven to be useful not only for modelling astrocytic buffering processes [25], but also other processes taking place in brain tissue at long time scales [54]. A natural aim for future work will be to generalize the formalism so that it can be applied to three-dimensional transport processes in brain tissue.

3.1.2 Astrocyte model

The KNP-framework (Fig. 3C) is general to the choice of membrane mechanisms (reflected in the transmembrane flux density j_{kM}). In the modelling study in [25], the astrocyte possessed the standard passive transmembrane fluxes of Na^+ (j_{Nap}) and Cl^- (j_{Clp}), a passive K^+ -flux (j_{Kir}) through the inward rectifying K^+ -channel, and the fluxes through the Na^+/K^+ -pump which exchanges 2 K^+ (inward) for 3 Na^+ ions (outward). The transmembrane fluxes of K^+ , Na^+ and Cl^- were, respectively

$$j_{KM} = j_{Kir} - 2P \quad (2)$$

$$j_{NaM} = j_{Nap} + 3P \quad (3)$$

$$j_{ClM} = j_{Clp}. \quad (4)$$

The expressions for j_{Kir} , j_{Nap} , j_{Clp} depend on the reversal potentials and conductances of the respective ion species, and the full expressions are given in the original work [25]. Also for the Na^+/K^+ -pump rate, P , we refer to the original work for the full expression [25].

3.1.3 Simulation setup

Below, we will present some simulations that explore how astrocytes transfer K^+ out from high-concentration regions. To induce such a high-concentration region, a selected region of the ECS (the *input zone* $0 < x < l/10$ as indicated in Fig. 3B) was exposed to a constant influx (j_{in}) of K^+ and a corresponding efflux of Na^+ . In this way, the external input to the system was locally electroneutral, so that no net charge was added to the system (otherwise, the electroneutrality constraint would be violated). We assumed that this input signal reflected the effect of intense local AP firing in the input zone, where neurons take up Na^+ and expel K^+ from/to the ECS. Furthermore, we also implicitly included the effect of neuronal uptake mechanisms, i.e., neurons that take up K^+ and expel Na^+ via exchanger pumps. Unlike j_{in} , these mechanisms were evenly distributed in the system, so that all points in space $0 < x < l$ experienced a K^+ -concentration

Table 1. Model parameters

Parameter	Explanation	Value/Units
k (index)	Ion species: K^+ , Na^+ or Cl^-	
n (index)	Domain: I (ICS) or E (ECS)	
a_I	Astrocyte volume per total tissue volume	0.4
a_E	ECS volume per total tissue volume	0.2
O_M	Astrocyte membrane area per total tissue volume	m^{-1}
l	Length of astrocyte	$300 \mu m$
z_k	Valence of ion species k	
$[k]_n$	Ion concentration of species k in domain n	mM
v_M	Membrane potential	mV
j_{kM}	Membrane flux density of species k	$\mu mol/(m^2 s)$
j_{kn}^f	Axial flux density due to electrical migration	$\mu mol/(m^2 s)$
j_{kn}^d	Axial flux density due to diffusion	$\mu mol/(m^2 s)$
j_{Kir}	Transmembrane K^+ flux density (Kir-channel)	$\mu mol/(m^2 s)$
j_{Nap}	Passive, transmembrane Na^+ flux density	$\mu mol/(m^2 s)$
j_{Clp}	Passive, transmembrane Cl^- flux density	$\mu mol/(m^2 s)$
P	Na^+/K^+ exchanger pump-rate	$\mu mol/(m^2 s)$
r_n	Resistivity	Ωm
D_K	K^+ diffusion constant	$1.96 \times 10^{-9} m^2/s$
D_{Na}	Na^+ diffusion constant	$1.33 \times 10^{-9} m^2/s$
D_{Cl}	Cl^- diffusion constant	$2.03 \times 10^{-9} m^2/s$
λ_I	intracellular tortuosity	3.2
λ_E	extracellular tortuosity	1.6
C_M	specific membrane capacitance	$1 \mu F/cm^2$
$\Delta[k]_n$	Deviance from baseline concentration	mM
$*[K^+]_E^0$	baseline ECS K^+ -concentration	3.082 mM
$*[K^+]_I^0$	baseline ICS K^+ -concentration	99.059 mM
$*[Na^+]_E^0$	baseline ECS Na^+ -concentration	144.622 mM
$*[Na^+]_I^0$	baseline ICS Na^+ -concentration	15.189 mM
$*[Cl^-]_E^0$	baseline ECS Cl^- -concentration	133.71 mM
$*[Cl^-]_I^0$	baseline ICS Cl^- -concentration	5.145 mM
$*v_{M0}$	initial membrane potential	-83.6 mV
k_{dec}	decay factor for $[K^+]_E$	$2.9 \times 10^{-8} m/s$
j_{in}	constant input in input zone	$7 \times 10^{-8} mol/(m^2 s)$

* Initial values correspond to the resting state of the model (static steady state in the case of no external input).

For the origin of the table values, see [25].

dependent decay towards the baseline ECS K^+ concentration $[K^+]_E^0$. The input function was

given by:

$$j_K^{in} = -j_{Na}^{in} = j_{in} - k_{dec}([K^+]_E - [K^+]_E^0). \quad (5)$$

Here, j_{in} is a constant input which was applied only in the input zone ($0 < x < l/10$) and in a selected time window ($100 \text{ s} < t < 400 \text{ s}$). The decay term was applied at all locations at all time. The decay factor (k_{dec}) and input flux density (j_{in}) are defined in Table 1.

The model was implemented in Matlab, and the code is publicly available at ModelDB (<https://senselab.med.yale.edu/ModelDB/ShowModel.cshtml?model=151945>). We only included the dynamics of the main charge carriers (K^+ , Na^+ and Cl^-), and the simulations were run with sealed-end boundary conditions (see [25] for details).

3.2 A mechanistic understanding of the K^+ -buffering process

Below, we aim to give a mechanistic picture of the K^+ -buffering process by presenting selected simulations from the original study [25]. We focus on mapping out the transport routes of K^+ , from entering to leaving the system, and on exploring how this depends on electrical forces, diffusive forces, and astrocytic uptake.

3.3 Ion concentration dynamics and steady state

In Fig. 4 we see how the extracellular ion concentrations (panel A), the intracellular ion concentrations (panel C), and v_M (panel E) changed after the input was turned on (at $t=100 \text{ s}$). It took the system roughly 30 seconds to reach steady state, after which the state variables remained at fixed values until the input was turned off (at $t=400 \text{ s}$). For ion concentrations, deviances from basal concentrations are shown. For example, $\Delta[K^+]_E$ was about 7.7 mM at steady state, corresponding to a concentration $[K^+]_E \simeq 10.8 \text{ mM}$ (as the baseline concentration was $\sim 3.1 \text{ mM}$). This value lies on the threshold between functional and pathological conditions [7, 9, 10], and is thus likely to represent a scenario where the K^+ buffering process is of paramount importance. Although the input was applied to the ECS of the input zone, $\Delta[K^+]_I \simeq 12.5 \text{ mM}$ was larger than $\Delta[K^+]_E$, reflecting the astrocyte's propensity for local K^+ -uptake. As has been also seen experimentally [5, 7, 55], the shifts in $[K^+]_E$ coincided with a local depolarization of the astrocytic membrane (panel E).

In the following we focus on the spatial aspect of the buffering process and limit the exploration to when the system is in steady state (the time $t=400 \text{ s}$ was selected for the steady-state situation). For all system variables, the deviation from the baseline conditions were biggest in the input zone, and generally decayed with increasing x (Fig. 4B,D,F). Note that the properties of the system lead to a rearrangement of Cl^- in the system, although Cl^- (unlike K^+ and Na^+) was not added/subtracted to/from the system. The gradients of both the ionic concentrations and electrical potential were quite pronounced, and we may thus expect that both diffusive and electrical forces contribute to transporting ions through the system (from entering to leaving). This is explored further in the following section.

3.4 System throughput during steady state

Figure 5 shows all the the ionic flows in the system during steady state. Due to the input configuration (Eq. 5) there was a net external influx of K^+ to the ECS in the input zone

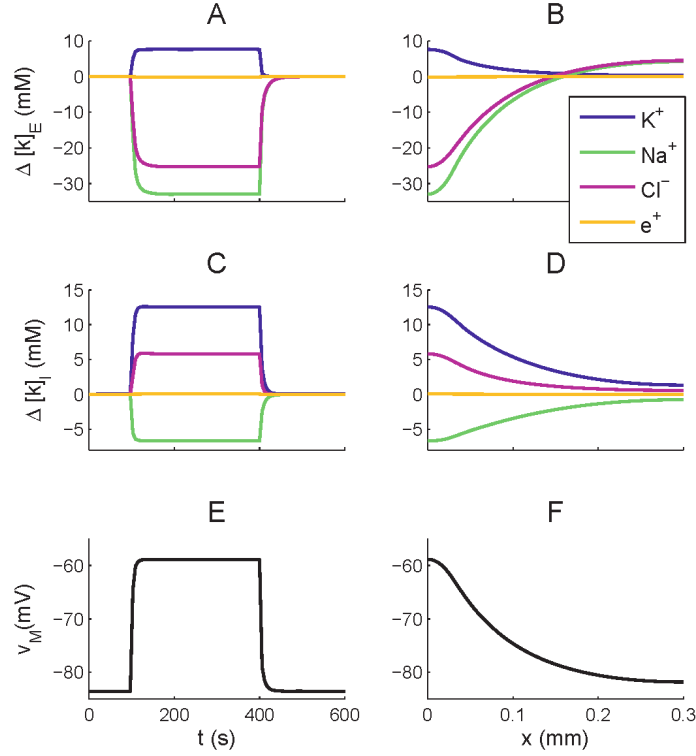


Figure 4. Dynamics and steady state profiles for the astrocyte/ECS-system. (A, C, E) Dynamics of selected variables in a point ($x = 0$) in the input zone. The constant cation-exchange input was applied to the ECS of the input ($0 < x < l/10$, $l=0.3$ mm) zone from $t = 100$ s to $t = 400$ s. During the input, ion concentrations in the ECS and ICS changed, but reached steady state after about 10-50 s after stimulus onset. $[K^+]_E$ (at $x = 0$) had then increased by about 7.7 mM with respect to the baseline value (A), while $[K^+]_I$ had increased by about 12.5 mM due to uptake by the astrocyte (C). The astrocytic membrane potential had been depolarized to about -59 mV at $x = 0$ (E). (B, D, F) Spatial profiles of selected variables at a time $t = 400$ s, when the system was in steady state. Deviations from the baseline ionic concentrations and v_M were smaller outside the input zone, and typically decreased with x . Far away from the input zone ($x \sim l=0.3$ mm), the conditions were close to the baseline conditions (A-D). Ionic concentrations were represented in terms of deviations from resting concentrations: $\Delta[k]_n = [k]_n - [k]_n^0$ for $n = I, E$. For direct comparison with ion concentrations, the charge density was represented as an equivalent concentration of unit charges $[e^+] = [K^+] + [Na^+] + [Cl^-]$. The figure was modified from [25].

($0 < x < l/10$), and a net efflux of K^+ at all points outside this region (Fig. 5A). As all external input/output was an electroneutral cation exchange, Na^+ and K^+ had opposite input profiles (compare blue and green curves).

Our main interest was on how the astrocyte influences the route that K^+ follows through the system. Fig. 5B shows how the transmembrane fluxes vary along the x -axis. The transmembrane

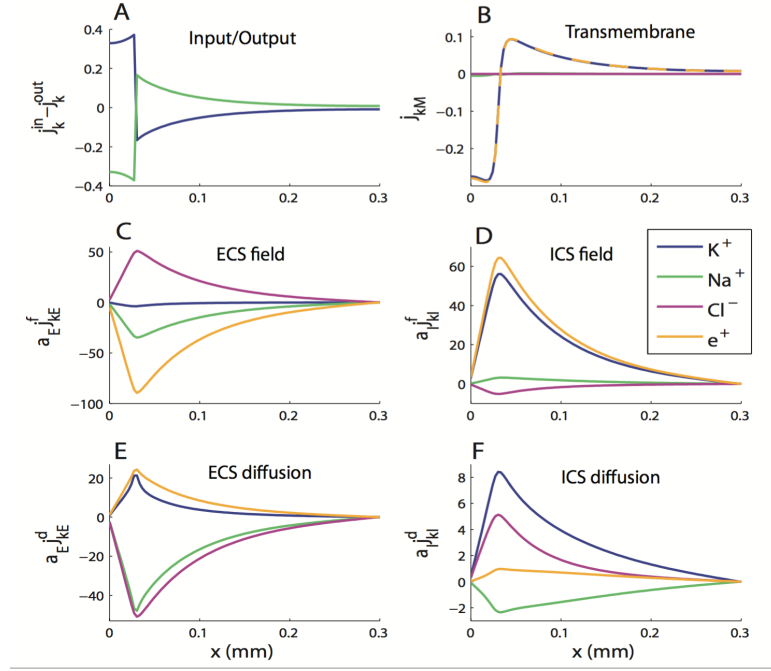


Figure 5. Ion transport in the astrocyte/ECS system at steady state. (A) Total flux densities into system (*input – output*). (B) Transmembrane flux densities. (C-F) Longitudinal flux densities due to (C) electrical migration in the ECS, (D) electrical migration in the ICS, (E) diffusion in the ECS and (F) diffusion in the ICS. (A-D) To aid comparison, flux densities j_{kn} were scaled by the relative area fraction a_n (e.g., if $a_E j_{kE} = a_I j_{kl}$, I and E carry the same net flux of ion species k). For direct comparison with ionic fluxes, the net electrical current was represented as a flux of positive unit charges $j_{e+} = j_{K+} + j_{Na+} - j_{Cl-}$. The input zone was in the region $0 < x < l/10$. Units on the y -axis are $\mu\text{mol}/(\text{m}^2\text{s})$ in all panels. The figure was modified from [25]

flux of K^+ (dark blue) was much larger than for Na^+ (green) and Cl^- (magenta). By definition, the transmembrane flux is negative for inward fluxes. According to Fig. 5B, there was thus a pronounced astrocytic uptake of K^+ in the high-concentration region, and a release outside this region.

To complete the picture of the spatial buffering process, we must also look at the intra- and extracellular fluxes of all ion species. To assess the relative roles of diffusion and electrical migration, we distinguished between field fluxes, which essentially reflect transports due to the extra- (Fig. 5C) and intracellular (Fig. 5D) voltage gradients in the system, and diffusive fluxes along the extra- (Fig. 5E) and intracellular (Fig. 5F) concentration gradients in the system. As expected, since the astrocyte absorbed K^+ in the input zone and released it outside this region (Fig. 5B), there was an intracellular longitudinal transport of K^+ in the positive x -direction. This transport was partly due to diffusion (Fig. 5F), as we could have predicted from the intracellular concentration gradient that we saw in Fig. 4D. However, due to the strong depolarization of the astrocyte in the input zone (Fig. 4F), electrical migration gave an even larger contribution

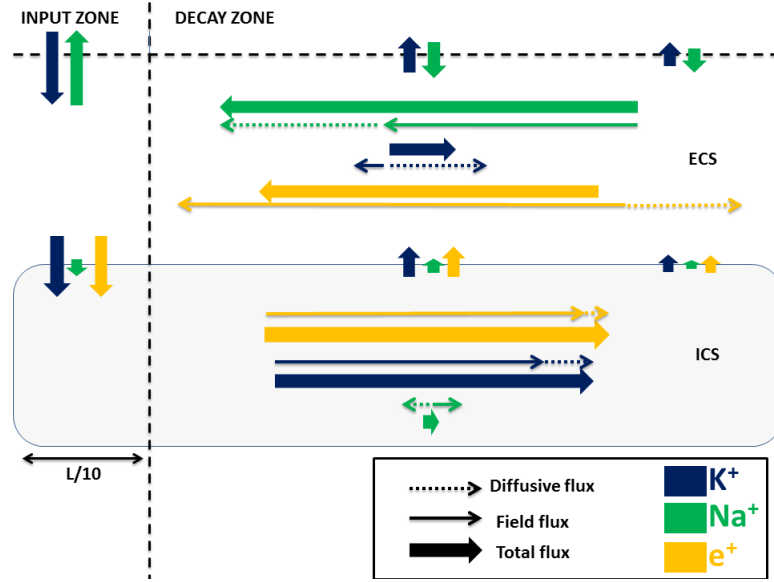


Figure 6. A flow chart of the ion transport in the astrocyte/ECS system at steady state.

A flow chart that qualitatively summarizes the essential information in Fig.5, showing the main transport routes of K^+ and Na^+ during steady state (Cl^- excluded from the overview). K^+ generally entered the system in the input zone and left the system from some point along the astrocyte axis. The transport route of K^+ (from entering to leaving the system) was predominantly intracellular, demonstrating the astrocyte's efficiency as a spatial buffer. Na^+ entered in the decay zone and left from the input zone. Na^+ transport predominantly took place in the ECS. The net electrical current cycled in the system. The illustration is qualitative - longer arrows mean higher flux densities, but the mapping from Fig.5 to the flow chart is not quantitatively exact. The figure was modified from [25]

to the intracellular transport of K^+ (Fig. 5D).

K^+ diffused in the positive x -direction also in the ECS (Fig. 5E). However, a depolarization of the astrocyte corresponded to a decrease in the ECS potential ($v_m = v_I - v_E$). Accordingly, the voltage gradient in the ECS drove K^+ in the negative x -direction (Fig. 5C). That is, diffusion and electrical migration were in the opposite direction in the ECS. This finding predicts that the astrocyte not only provides an additional and more effective domain for longitudinal K^+ -transport, but even reduces the net transport of K^+ through the ECS, thus shielding the ECS from K^+ .

Figure 6 qualitatively summarizes the ionic flows through the system during steady state. K^+ entered the system in the ECS of the input zone, where a major fraction of it crossed the membrane, was transported intracellularly in the positive x -direction, and was released to the ECS at higher x -values, from where it eventually left the system (via neuronal uptake). Whereas the main transport route for K^+ was intracellular, the situation for Na^+ was opposite. Na^+ entered the system outside the input zone, and was predominantly transported in the negative x direction through the ECS, and left the system in the input zone (neuronal AP firing). The net Cl^- transport was very small (flux densities due to diffusion and electrical migration canceled each others out) and was not included in Fig.6.

The simulations shown here illustrate that K^+ -buffering depends on a fine interplay between electrical and diffusive transport processes, and could thus not be reliably simulated without a consistent electrodiffusive modelling scheme, such as the KNP-framework. We conclude that astrocytes seem tailored for shielding the ECS from excess K^+ . In the original work [25], we also showed that K^+ clearance from high concentration was much more efficient when astrocytes were present than in the case of a correspondingly enlarged ECS, a hypothesis that had been posed earlier, but not yet tested [56].

4 Microscale water flow

A striking difference between astrocytes and neurons is that astrocytes have water specific channels, aquaporin-4 (AQP4), embedded in the membrane. In the astrocytic end-feet, i.e., the processes that reach out and collectively create a sheath around the blood vessels and towards the pial surface, the AQP4 density has been reported to be as high as $2400/\mu m^2$ (see Furman et al. [57] Fig. 6). At the astrocytic membrane facing neuropil the AQP4 density is about a factor 20 lower [58], but this is still dense compared to standard ion channel densities: in neurons the sodium channel densities is estimated to be about $1/\mu m^2$ in the cell body and about $100/\mu m^2$ to $200/\mu m^2$ in the densest regions such as the axon hillock [59].

Throughout the body the lymphatic system removes excess fluid and waste from the tissue, but there is no lymphatic system within neuropil, although lymph vessels were recently discovered within the meningeal compartment [60]. This lack of lymph system within the neuropil led Iliff et al. [61] to suggest a 'glymphatic pathway' – the brain's counterpart to a lymphatic pathway – between the vasculature and the astrocyte end-feet, i.e., that a flow of water through the interstitial space directed from the periarterial space to the perivenous space (see Fig. 7E) functions as a clearance mechanism for waste products such as amyloid beta. AQP4 deletion has shown to reduce clearance of amyloid beta by 65% [61], and thus AQP4 seems to play an important role in the 'glymphatic system'.

The role of astrocytic AQP4 in potassium buffering is controversial [62–64]. Here, we show how AQP4 can both stabilize the extracellular concentration of solutes and possibly also induce a convective water flow. We also show that there is a possible interplay between osmotic forces and water fluxes through AQP4 interactions, which may be important for both potassium buffering and for the glymphatic system.

4.1 Transport mechanisms

The osmotic pressure over the membrane is strong compared to typical hydrostatic pressures (see Subsection 4.2). Upon osmotic changes, water flow through the high density of AQP4 in the astrocyte membrane and reestablishes the osmotic balance between the ECS and the intracellular volume of the astrocytes within milliseconds [65]. Depending on cortical state, this may lead to swelling or shrinkage of the astrocytes. Xie et al. [66] found that during sleep the extracellular volume increases by about 60% and that this increase in volume leads to a better clearance of amyloid beta due to an increased convective flow through the ECS. Although osmosis may regulate the ECS volume and thereby the convective flow, it is not clear whether osmosis is a

driving force for the flow itself. Cerebral arterial pulsation has, however, been demonstrated to be a key driver for this flow [67].

Many aspects of the glymphatic system are not understood, and the concept itself is still debated [68–70]. However, for water to be driven through the interstitial space, from the periarterial to the perivenous space, either hydrostatic or osmotic pressure gradients must act as driving forces. Note, however, that the osmotic pressure and the hydrostatic pressure acts very differently: the hydrostatic pressure may cause pressure difference between any two extracellular (or intracellular) sites, whereas the osmotic pressure acts over membranes.

If we assume an elevated hydrostatic pressure in the periarterial space compared to the perivenous space, there will be a net hydrostatic pressure gradient over the end-feet layers and through the interstitial space (see black arrows in Fig. 7E). This may cause an extracellular flow, and the convection may serve as a clearance mechanism for amyloid beta and other waste products.

In Fig. 7, we have calculated pressure gradients in the astrocyte/ECS model presented in Section 3, using identical parameters and input conditions as there. The changes in ionic concentrations induced by the input (cf. Eq. 5), were most dramatic in the input zone. In Fig. 7B, the summed intracellular and ECS concentrations are shown at different time points after the input was turned on. The concentration shifts gave rise to a maximal, activity-induced change in osmolality of more than 60 mOsm/L, i.e., the induced change in concentrations between the intracellular and extracellular sites was more than 60 mM. The pressure shift was largest in the input zone, where the shift in osmotic pressure across the membrane was about 1000 mmHg (see Fig. 7C, see also Eq. 8 for the formula for osmotic pressure). Further, the spatial extension of the cable lead to an osmotic gradient along the membrane.

We did not explicitly include water flow in the modelling framework, but the observations in Fig. 7 allow us to make some qualitative predictions from the pressure gradients. Firstly, from the osmotic pressure in the input zone, we would predict a local influx of water, which would lead to astrocyte swelling [28]. Secondly, depending on the membrane elasticity, a hydrostatic pressure would build up intracellularly, and cause an intracellular water flow away from the input zone. Fig. 7E illustrates two different flow patterns that we would expect if astrocytes were either connected to the arterial site (left) or to the venous site (right). The high intracellular pressure would cause an intracellular water flux out from the input zone (orange arrows), directed both towards the arterial site and towards the venous site, depending on astrocyte density, their connections to the vasculature, their respective AQP4 densities et cetera. In Fig. 7E black arrows indicate the expected flow caused by arterial pulsation and pressure differences between the periarterial and perivenous spaces.

As of now, it is still an open question whether K^+ buffering evokes osmotic forces strong enough to produce a convective flow of considerable magnitude. In general, it is not clear whether the net extracellular convective flow is mainly driven by arterial pulsation or by osmotic forces. Experiments show that both AQP4 and arterial pulsation are important for the glymphatic flow: for AQP4 deletion clearance of amyloid beta was reduced by 65% [61], and Iliff et al. [67] suggested that cerebral arterial pulsatility is a key driver of paravascular CSF influx into and through the brain parenchyma. It is presently not possible to measure the small hydrostatic pressure differences within the tiny astrocytic compartments. Thus, to understand the role of osmotic forces in potassium buffering a tight interplay between experiments and

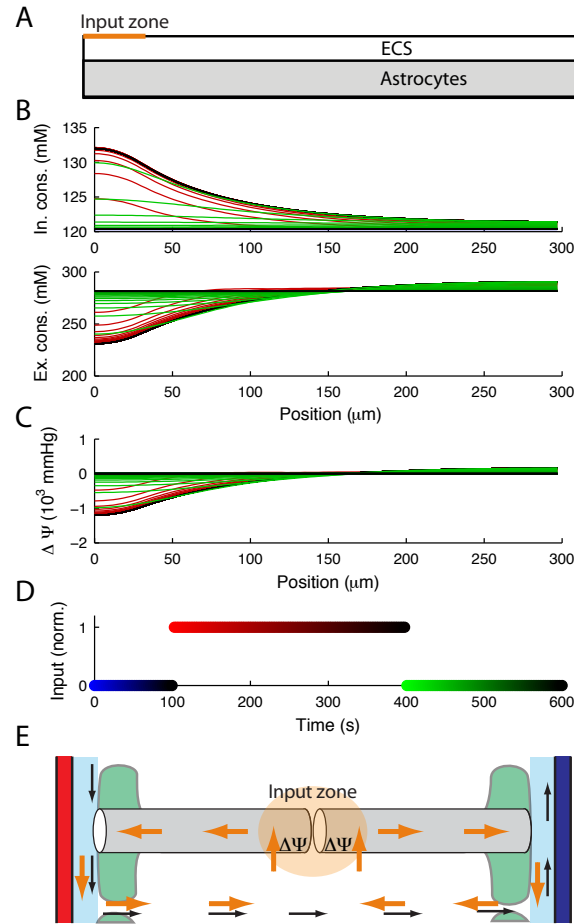


Figure 7. Illustration of how the astrocyte machinery may generate an osmotic gradient following neural activity and induce water flow into the astrocyte. The model shown in Fig. 3 is run with default parameters. (A) Illustration of the electrodiffusion model, see Fig. 3 for details. At time $t = 100$ s the model is triggered by neural activity (decreased extracellular Na^+ and increased extracellular K^+) within the input zone. (B) The spatial distribution of net concentration of intracellular (upper) and extracellular ions (lower), leading to change in osmotic pressure seen in (C). The osmotic pressure is here assumed to be zero in equilibrium. (D) The color coding of (B) and (C) depicts time. Input is given in red, bright red at the beginning of the input, darker towards the end, whereas times after the 300 s input stimulus is turned off is shown in green. (E) An assumed system of two types of astrocytes, one type approaching the arterial site, the other type approaching the venous site. Red (left) is the arterial site, blue (right) is the venous site. The end-feet, shown in green, cover the vasculature and define perivascular spaces filled with water (light blue) along both arterioles and venules. Osmotically induced flow pattern depicted with orange arrows, and the hypothesized hydrostatic flow with black arrows. Note that the hydrostatic flow may go both through the end-feet and through the tiny clefts between end-feet.

modelling is needed. This also applies to the glymphatic system and the question of clearance of waste products. Future astrocyte models with spatial extension should emphasize to incor-

porate not only electrodiffusion, but also the convective flow caused both by osmotic pressures and by hydrostatic pressure originating from arterial pulsation or respiration. Such a complete modelling framework is not available yet, but below we assess some of the key ingredients that it will need.

4.2 Osmosis and astrocyte swelling

Above we showed some qualitative results of possible convective flows, both extracellularly and intracellularly in astrocytes. Here we will give quantitative estimates of the strength of the osmotic forces, the water flow, and the typical time scale for this mechanism.

The lipid bilayer without AQP4 channels has a rather low water permeability compared to the permeability of the astrocyte with a normal AQP4 density [71]. As an additional boosting effect, AQP4 is often arranged in so-called orthogonal arrays. These arrays may increase the collective permeability of AQP4 as much as 10 times compared to the sum of the single channel permeabilities [71], and orthogonal arrays are especially prominent within the astrocyte end-feet.

The membrane permeability, which is determined by the density of AQP4, has a direct impact on how fast the ECS volume can be regulated upon osmotic stress. In Tong et al. [65] the ECS osmolarity was manipulated, and the cells swelled until they reached a new equilibrium. The swelling was fitted to exponential functions, and the estimated time constants were as small as $\tau = 1/(120.5 \text{ s}^{-1}) \approx 8.3 \text{ ms}$ for cells with high densities of AQP4. Thus, astrocytes should be able to adjust to sudden changes in osmotic stress within milliseconds. A rapid swelling of astrocytes would serve to regulate the ECS osmolarity, thereby stabilizing the ECS environment and presumably preventing osmotic pressure differences to cause swelling of neurons, as neurons do not have AQP4 water channels and thus have a much longer time constant for water inflow.

Below we describe the basic formalism for osmotically induced swelling of astrocytes. Note that a similar formalism has been integrated with single compartment models of ion dynamics (see e.g., [18,28]), but not yet in spatially extended models.

4.2.1 Basic formalism for osmotically induced volume changes

Similarly to Ohm's law for electricity, Darcy's law defines the water flow Q as a product of the permeability G_{tot} and the pressure difference $\Delta\Psi$,

$$Q = G_{\text{tot}} \Delta\Psi , \quad (6)$$

where Q has units of m^3/s , $\Delta\Psi$ has units of Pa and G_{tot} has units of $\text{m}^3/\text{s}/\text{Pa}$. We use the symbol Ψ for the water potential, since flow across a membrane is caused both by hydrostatic and osmotic pressure differences over the membrane,

$$\Psi = \Psi_p + \Psi_{\Pi} . \quad (7)$$

Here Ψ_{Π} is called the solute potential, and the hydrostatic pressure (the pressure potential) is denoted Ψ_p . Differences in the solute potential over the membrane correspond to the osmotic pressure. Both Ψ_{Π} and Ψ_p have units of Pascal. Water flows from a high water potential to a lower water potential, and the solute water potential is defined to be zero for pure water and is negative for any solute.

If we assume ideal solutions with low concentrations of solutes, we can use the Morse equation to compute the solute potential [72]:

$$\Psi_{\Pi} = iMRT . \quad (8)$$

Here i is the ionization factor (van't Hoff factor), i.e., the ratio between the actual concentration of particles produced when the substance is dissolved, and the concentration of a substance as calculated from its mass, $R \approx 8.3 \text{ J}/(\text{mol K})$ is the gas constant, T , here assumed to be 310 K, is the absolute temperature, and M is the osmotic concentration of solutes measured in moles per litre. Our solutes are here assumed to be ions, thus $i = 1$.

If we combine Eqs. 6 and 8, assume the hydrostatic pressure Ψ_p to be the same at both sides of the membrane, and notice that Q is the flow rate of the extracellular volume V_e across the membrane and into the intracellular volume, i.e., $Q = dV_e/dt$, the volume dynamics is given by

$$\frac{dV_e}{dt} = -RTGA \left(\frac{N_a}{V - V_e} - \frac{N_e}{V_e} \right) . \quad (9)$$

Here N_e and N_a are the number (moles) of extracellular and intracellular (astrocytic) solutes, respectively, and $V = V_e + V_a$ is the sum of the ECS and astrocyte volumes. We have expressed the total membrane permeability G_{tot} from Eq. 6 as $G_{\text{tot}} = GA$, where G is the permeability per membrane area and A is total membrane area within the volume V . If we assume the volume V and the number of ions N_e and N_a to be constants, a general solution can be written

$$-tRTGA = \frac{N_a V V_e}{(N_a + N_e)^2} - \frac{V_e^2}{2(N_a + N_e)} + \frac{N_a N_e V^2 \ln([N_a + N_e]V_e - N_e V)}{(N_a + N_e)^3} + C , \quad (10)$$

where C is an integration constant. This expression cannot be converted into a simple formula for V as a function of the time t , but for typical parameters (see Subsection 4.2.2), we find that the logarithmic term dominates the right hand side of the equality. Thus, an approximate solution can be written on a simple functional form as

$$\frac{V_e}{V} \approx \tilde{C} e^{-t/\tau} + \tilde{N}_e , \quad (11)$$

with the constant $\tilde{C} = V_0/V - \tilde{N}_e$, where V_0 is the initial extracellular volume and $\tilde{N}_e = N_e/(N_e + N_a)$ is the relative extracellular number fraction. The time constant is given by

$$\tau = \frac{N_a N_e V^2}{(N_e + N_a)^3 RTGA} = \frac{\tilde{N}_a \tilde{N}_e}{c RTGA/V} . \quad (12)$$

In the last equality we have used the relative number fractions \tilde{N}_e and $\tilde{N}_a = N_a/(N_e + N_a)$, and c is the net concentration of solutes within V , i.e., $c = (N_e + N_a)/V$. From the expression we find that the time constant is inversely proportional to the volume density A/V of AQP4.

4.2.2 Experimentally extracted parameters

Based on experimentally measured quantities, we will in this subsection estimate typical the transmembrane water flow and the time constant τ , derived in Eq. 12, for astrocytes. The most important parameters are found in Table 2.

Table 2. Model parameters, Section 4.

Parameter	Explanation	Value/Units
\tilde{N}_a	fraction of intracellular ions	0.55
\tilde{N}_e	fraction of extracellular ions	0.45
c	net solute concentration $c = (N_a + N_e)/V$	300 mOsm/L
R	gas constant	8.314 LkPa/K/mol
T	absolute temperature	310 K
P_f	osmotic permeability per unit area	0.01 cm/s
G	water permeability per unit area	7.0×10^{-13} m/s/Pa
ΔM	concentration difference of solutes	60 mol/m ³ = 60 mM
M_w	molarity of water	55.5 mol/L = 55.5 M
Q_m	molar flux	mol/s
Q	transmembrane water flow	m ³ /s
A/V	area to volume fraction	20 $\mu\text{m}^2/\mu\text{m}^3$

Estimates of the AQP4 water-channel permeability are typically based on osmotic permeability experiments relating the concentration difference ΔM (in units of mol/m³) of impermeable molecules between two sides of a cell membrane, to the molar flux Q_m of water through the membrane,

$$P_{f,\text{cell}} = Q_m / \Delta M . \quad (13)$$

The molar flux Q_m can be estimated from cell swelling measurements. Further, the single channel AQP4 permeability or the permeability per unit area can be estimated by additional electron microscopy of the density of AQP4 channels within the membrane [65]. If we assume the hydrostatic pressure Ψ_p to be the same at both sides of the membrane, the correspondence between reported osmotic permeability per unit area P_f and the permeability per unit area $G = G_{\text{tot}}/A$ where A is the membrane area, is found by substituting Eqs. 8 and 13 into Eq. 6. This gives

$$G = P_f / (RTM_w) , \quad (14)$$

with $M_w = Q_m/Q$ denoting the molarity of water.

The permeability per unit area G was used in Eq. 10 to relate the volumetric flow rate $Q = dV_e/dt$ through the membrane to the osmotic pressure difference, and it was shown that its value is inversely proportional to the time constant τ , see Eq. 12. Based on data for the relative density of AQP4 in end-feet vs. the membrane facing neuropil [58], as well as estimates for both P_f [71, 73] and single channel permeability [65, 74], we use $P_f = 0.01$ cm/s to arrive at a numerical value for the time constant τ .

The total neuronal membrane area is estimated to be 25000 m² for human [75, p. 97] and the brain volume is about 1350 cm³. This leads to a membrane area to volume density of 18.5 $\mu\text{m}^2/\mu\text{m}^3$. A similar density can be found for mouse. We assume a default value for the volume density of astrocytic membrane area to be similar to the volume density of neuronal membrane area, i.e., $A/V = 20$ $\mu\text{m}^2/\mu\text{m}^3$.

We further assume increased osmotic pressure equivalent to 1000 mmHg within a cube of sides $100\text{ }\mu\text{m}$. According to our assumptions this volume will contain $A_m = 2 \cdot 10^7\text{ }\mu\text{m}^2$ of membrane area. The osmotic pressure corresponds to a concentration difference of less than 60 mOsm/L between the inside and the outside of the membrane, cf. Eq. 8. The net rate of water influx to the astrocytes within the volume is then

$$Q = GA_m \Delta\Psi = 0.002\text{mm}^3/\text{s} . \quad (15)$$

This initial influx rate corresponds to twice the total volume V per second, and for a standard extracellular volume fraction of 20 % it corresponds to a net influx rate of 10 times the ECS volume per second. However, as water moves from the ECS to the intracellular space, the osmotic pressure will be reduced according to Eq. 10. If we assume both the ECS and the astrocytic volume fraction to be 20% of the total volume [76], the astrocytic osmolarity to be 330 mOsm/L, and the extracellular osmolarity to be 270 mOsm/L, the system will, according to Eqs. 11 and 12, reach equilibrium when the extracellular volume fraction is 18% and the intracellular is 22%, and the time constant will be $\tau = 9.2\text{ ms}$. This is in good agreement with experimental results from Tong et al. [65].

These simple considerations show that the osmotic response to neural activity is fast and the transmembrane influx rate of water may be substantial.

5 Macroscale fluid flow through brain tissue

Fluid flow through the central nervous system is inherently of a multiscale character and thus amenable to a multitude of modelling approaches, for a recent review in the context of biomechanics see, e.g., [77]. At the macroscale, that is, at the whole brain scale, three distinctive approaches to the continuum modelling of fluid and solute flow through the brain tissue are: (i) single or multiple-network poroelasticity theory, (ii) direct modeling and coupling of the interstitial tissue flow with free flow (Darcy-Stokes flow) [78], and (iii) coupling the microcirculation (vasculature) with the tissue itself via one-dimensional networks (Darcy flow with embedded Navier-Stokes flow) [79]. Of these, the first approach has gained momentum for the biomechanical modelling of fluid flow through brain tissue and also through the spinal cord, see e.g., [77] and references therein.

These single- and multiple-network poroelasticity theories originally originate from geoscience [80,81], but have been proposed to model the flow and exchange of fluid through biological tissue in general and the brain in particular [82]. The theory is based on modeling the tissue as a solid matrix permeated by interconnecting multiple pathways or networks where each network is characterized by its porosity. For instance, Vardakis et al [83] consider a model incorporating the intracellular space permeated by four networks corresponding to the arteries, the arterioles/capillaries, the veins and the extracellular space respectively. In the case of a single fluid network (here, the extracellular space) and under the assumptions of linear tissue elasticity, isotropy, and incompressibility, the general multiple-network poroelasticity model reduces to the well-known Biot equations [80]. In addition, to modelling the flow of interstitial fluid through the tissue itself, computational models typically also need to account for the interplay with the cerebrospinal fluid flow in the subarachnoid spaces and ventricles as illustrated by, e.g., [83–85].

The multiple-network poroelasticity equations, in the absence of local body forces, sources or sinks, and inertial terms, and assuming incompressible fluid networks for the sake of simpler presentation, take the form [82]: find the spatially and temporally varying tissue deformation u and the pressures p_a for each network $a = 1, \dots, A$ such that

$$-\nabla \cdot \sigma(u) + \sum_a \nabla p_a = 0, \quad (16)$$

where σ is the stress tensor, for instance given by Hooke's law under the assumptions of linearly deforming elastic tissue, and for each $a = 1, \dots, A$:

$$\nabla \cdot \dot{u} - \nabla \cdot (G_a \nabla p_a) = \sum_{b \neq a} s_{b \rightarrow a}. \quad (17)$$

In Eq. 17, $G_a = \kappa_a / \mu_a$ where κ_a is the permeability and μ_a the viscosity of network a . The exchange coefficients $s_{b \rightarrow a}$ govern the rate of transfer from network b to network a and are subject to modelling. The fluid velocity in network a is defined in terms of the network pressure p_a by:

$$v_a = -G_a \phi_a^{-1} \nabla p_a, \quad (18)$$

where ϕ_a is the porosity or volume fraction of network a which, note, may or may not be spatially varying.

The multiple-network poroelasticity framework is attractive in that it allows for specific incarnations, at different levels of complexity, and modelling fluid flow in, e.g., the different compartments of the 'glymphatic system'. Variations in the extracellular and astrocytic volume fractions, cf. Section 4.2, are naturally modelled via the network porosities, while microscale water flow and AQP4 densities, as discussed in Section 4, govern the dynamics of the exchange coefficients.

6 Concluding remarks

The recent years have seen the launching of several ambitious large-scale projects aiming to link the different scales in the brain, from molecules to systems. Prominent examples are EUs Human Brain Project, the US BRAIN Initiative and Project MindScope at Allen Institute of Brain Sciences [86]. Here computational neuroscience will play a key role in integrating neurobiological data, storing current knowledge, and testing hypotheses by means of a set of interconnected mathematical models together bridging the different scales. The main focus of these projects is to understand the information processing in the brain, and a central goal is to link processing and spiking activity at the single-neuron level to systems level measures of neural activity such as the local field potential (LFP) [87], electroencephalography (EEG) [88], or magnetoencephalography (MEG) [89].

In these projects the astrocytes will be secondary to the neurons as their main role is likely to be of a homeostatic nature, i.e., to provide the neurons with stable environments for their information processing. An example is the presently discussed role of astrocytes in providing spatial K^+ buffering to maintain low concentrations of potassium in the ECS and avoid pathological neuronal firing.

Another multiscale brain project is to try to link neural activity to macroscopic fluid flow. Here astrocytes will likely be at center stage as their ion-concentration dynamics appear to provide a key connection to fluid flow via osmotic effects. In the current work, we have outlined some elements that we believe will be of key importance for this multiscale approach: In Section 2 we discussed how neuronal and astrocytic dynamics are linked via ions in ECS, in Section 3 we described the recently introduced Kirchoff-Nernst-Planck (KNP) scheme for modeling ion dynamics in astrocytes (and brain tissue in general), in Section 4 we described how astrocytes may regulate microscopic liquid flow by osmotic effects, and in Section 5 we finally discussed how such microscopic flow can be linked to whole-brain macroscopic flow.

A long-term ultimate goal would be to make joint multiscale, multimodal models for brain tissue including both information processing by spikes, liquid flow, hemodynamic activity and metabolic activity [90]. Such models could not only become invaluable mathematical "microscopes" for exploring brain function but also hopefully become important tools for understanding brain pathologies and suggest new treatments.

References

1. Wang DD, Bordey A (2008) The astrocyte odyssey. *Progress in neurobiology* 86: 342–67.
2. Somjen GG (2004) *Ions in the Brain: Normal Function, Seizures, and Stroke*. Oxford University Press, USA, 1 edition.
3. Frankenhaeuser B, Hodgkin AL (1956) The after-effects of impulses in the giant nerve fibres of loligo. *J Physiol* 131: 341–76.
4. Cordingley G, Somjen G (1978) The clearing of excess potassium from extracellular space in spinal cord and cerebral cortex. *Brain research* 151: 291–306.
5. Dietzel I, Heinemann U, Lux H (1989) Relations between slow extracellular potential changes, glial potassium buffering, and electrolyte and cellular volume changes during neuronal hyperactivity in cat. *Glia* 2: 25–44.
6. Gardner-Medwin A (1983) Analysis of potassium dynamics in mammalian brain tissue. *The Journal of physiology* : 393–426.
7. Chen KC, Nicholson C (2000) Spatial buffering of potassium ions in brain extracellular space. *Biophysical journal* 78: 2776–97.
8. Haj-Yasein NN, Bugge CE, Jensen V, Ostby I, Ottersen OP, et al. (2014) Deletion of aquaporin-4 increases extracellular K(+) concentration during synaptic stimulation in mouse hippocampus. *Brain structure & function* 220: 2469–74.
9. Hertz L, Xu J, Song D, Yan E, Gu L, et al. (2013) Astrocytic and neuronal accumulation of elevated extracellular K⁺ with a 2/3 K⁺/Na⁺ flux ratio consequences for energy metabolism, osmolarity and higher brain function. *Frontiers in Computational Neuroscience* 7: 1–22.
10. Newman EA (1993) Inward-rectifying potassium channels in retinal glial (Müller) cells. *The Journal of neuroscience : the official journal of the Society for Neuroscience* 13: 3333–45.
11. Syková E, Nicholson C (2008) Diffusion in Brain Extracellular Space. *Physiol Rev* 88: 1277–1340.
12. Enger R, Tang W, Vindedal GF, Jensen V, Johannes Helm P, et al. (2015) Dynamics of Ionic Shifts in Cortical Spreading Depression. *Cerebral cortex (New York, NY : 1991)* : 1–8.

13. Park EH, Durand DM (2006) Role of potassium lateral diffusion in non-synaptic epilepsy: a computational study. *Journal of theoretical biology* 238: 666–82.
14. Florence G, Dahlem MA, Almeida ACG, Bassani JWM, Kurths J (2009) The role of extracellular potassium dynamics in the different stages of ictal bursting and spreading depression: a computational study. *J Theor Biol* 258: 219–228.
15. Somjen GG (2001) Mechanisms of spreading depression and hypoxic spreading depression-like depolarization. *Physiological reviews* 81: 1065–1096.
16. Orkand RK, Nicholls JG, Kuffler SW (1966) Effect of nerve impulses on the membrane potential of glial cells in the central nervous system of amphibia. *Journal of neurophysiology* 29: 788–806.
17. Lux HD, Heinemann U, Dietzel I (1986) Ionic changes and alterations in the size of the extracellular space during epileptic activity. *Adv Neurol* 44: 619–39.
18. Øyehaug L, Østby I, Lloyd CM, Omholt SW, Einevoll GT (2012) Dependence of spontaneous neuronal firing and depolarisation block on astroglial membrane transport mechanisms. *J Comput Neurosci* 32: 147–165.
19. De Keyser J, Mostert JP, Koch MW (2008) Dysfunctional astrocytes as key players in the pathogenesis of central nervous system disorders. *Journal of the neurological sciences* 267: 3–16.
20. Nedergaard M, Dirnagl U (2005) Role of glial cells in cerebral ischemia. *Glia* 50: 281–6.
21. Kríz N, Syková E, Vyklický L (1975) Extracellular potassium changes in the spinal cord of the cat and their relation to slow potentials, active transport and impulse transmission. *The Journal of physiology* 1: 167–182.
22. Lothman E, Somjen G (1975) Extracellular potassium activity, intracellular and extracellular potential responses in the spinal cord. *The Journal of physiology* 1: 115–136.
23. Coles J, Orkand R (1986) Free Concentrations of Na, K, and Cl in the Retina of the Honeybee Drone: StimulusInduced Redistribution and Homeostasis. *Annals of the New ...* 481: 303–317.
24. Nicholson C, Chen K, Hrabětová S, Tao L (2000) Diffusion of molecules in brain extracellular space: theory and experiment. *Progress in brain research* 125: 129–154.
25. Haldnes G, Ostby I, Pettersen KH, Omholt SW, Einevoll GT (2013) Electrodifusive model for astrocytic and neuronal ion concentration dynamics. *PLoS computational biology* 9: e1003386.
26. Macaulay N, Zeuthen T (2012) Glial K clearance and cell swelling: key roles for cotransporters and pumps. *Neurochemical research* 37: 2299–309.
27. Kofuji P, Newman EA (2004) Potassium buffering in the central nervous system. *Neuroscience* 129: 1045–56.
28. Østby I, Øyehaug L, Einevoll GT, Nagelhus EA, Plahte E, et al. (2009) Astrocytic mechanisms explaining neural-activity-induced shrinkage of extraneuronal space. *PLoS Comp Biol* 5: e1000272.
29. Ullah G, Schiff S (2009) Models of epilepsy. *Scholarpedia* 4: 1409.
30. Hübel N, Dahlem MA (2014) Dynamics from Seconds to Hours in Hodgkin-Huxley Model with Time-Dependent Ion Concentrations and Buffer Reservoirs. *PLoS Comput Biol* 10: e1003941.
31. Kager H, Wadman WJ, Somjen GG (2000) Simulated seizures and spreading depression in a neuron model incorporating interstitial space and ion concentrations. *J Neurophysiol* 84: 495–512.
32. Kager H, Wadman WJ, Somjen GG (2006) Seizure-like afterdischarges simulated in a model neuron. *J Comput Neurosci* 22: 105–128.

33. Cressman J, Ullah G, Ziburkus J, Schiff S, Barreto E (2009) The influence of sodium and potassium dynamics on excitability, seizures, and the stability of persistent states: I. single neuron dynamics. *J Comput Neurosci* .
34. Somjen GG, Kager H, Wadman WJ (2008) Computer simulations of neuron-glia interactions mediated by ion flux. *Journal of computational neuroscience* 25: 349–65.
35. Sibille J, Duc KD, Holcman D, Rouach N (2015) The neuroglial potassium cycle during neurotransmission: role of kir4. 1 channels. *PLoS Comput Biol* 11: e1004137.
36. Jensen MS, Yaari Y (1997) Role of intrinsic burst firing, potassium accumulation, and electrical coupling in the elevated potassium model of hippocampal epilepsy. *J Neurophysiol* 77: 1224–33.
37. Ziburkus J, Cressman JR, Barreto E, Schiff SJ (2006) Interneuron and pyramidal cell interplay during in vitro seizure-like events. *J Neurophysiol* 95: 3948–54.
38. Grisar T, Guillaume D, Delgado-Escueta AV (1992) Contribution of Na⁺,K⁽⁺⁾-ATPase to focal epilepsy: a brief review. *Epilepsy Res* 12: 141–149.
39. Verkhratsky A, Butt AM (2013) Glial physiology and pathophysiology. John Wiley & Sons.
40. Zhang Y, Barres BA (2010) Astrocyte heterogeneity: an underappreciated topic in neurobiology. *Current opinion in neurobiology* 20: 588–594.
41. Destexhe A, Bal T, McCormick DA, Sejnowski TJ, Sejnowski J, et al. (1996) Ionic mechanisms underlying synchronized oscillations and propagating waves in a model of ferret thalamic slices. *J Neurophysiol* 76: 2049–2070.
42. Halmes G, Augustinaite S, Heggelund P, Einevoll GT, Migliore M (2011) A multi-compartment model for interneurons in the dorsal lateral geniculate nucleus. *PLoS Comput Biol* 7: e1002160.
43. Rall W (1977) Core conductor theory and cable properties of neurons. In: Kandel E, Brookhardt J, Mountcastle VM, editors, *Handbook of Physiology*, Bethesda: American Physiological Society, chapter 3. pp. 39–97. URL <http://onlinelibrary.wiley.com/doi/10.1002/cphy.cp010103/full>.
44. Koch C (1999) *Biophysics of computation: information processing in single neurons*. Oxford University Press: New York, 1st edition.
45. Qian N, Sejnowski T (1989) An electro-diffusion model for computing membrane potentials and ionic concentrations in branching dendrites, spines and axons. *Biological Cybernetics* 15: 1–15.
46. Odette L, Newman EA (1988) Model of potassium dynamics in the central nervous system. *Glia* 210: 198–210.
47. Léonetti M, Dubois-Violette E (1998) Theory of Electrodynamical Instabilities in Biological Cells. *Physical Review Letters* 81: 1977–1980.
48. Lu B, Zhou YC, Huber Ga, Bond SD, Holst MJ, et al. (2007) Electrodifusion: a continuum modeling framework for biomolecular systems with realistic spatiotemporal resolution. *The Journal of chemical physics* 127: 135102.
49. Lopreore CL, Bartol TM, Coggan JS, Keller DX, Sosinsky GE, et al. (2008) Computational modeling of three-dimensional electrodiffusion in biological systems: application to the node of Ranvier. *Biophysical journal* 95: 2624–35.
50. Nanninga PM (2008) A computational neuron model based on Poisson Nernst Planck theory. *ANZIAM J* 50: 46–59.

51. Pods J, Schönke J, Bastian P (2013) Electrodifusion models of neurons and extracellular space using the Poisson-Nernst-Planck equations—numerical simulation of the intra- and extracellular potential for an axon model. *Biophysical journal* 105: 242–54.
52. Mori Y (2009) From Three-Dimensional Electrophysiology to the Cable Model : an Asymptotic Study. arXiv:09013914 [q-bioNC] : 1–39.
53. Grodzinsky F (2011) *Fields, Forces, and Flows in Biological Systems*. Garland Science, Taylor & Francis Group, London & New York.
54. Halnes G, Mäki-Martutunen T, Keller D, Pettersen KH, Einevoll GT (2015) The effect of ionic diffusion on extracellular potentials in neural tissue. arXiv:150506033 .
55. Newman EA (1987) Distribution of potassium conductance in mammalian Muller (glial) cells: a comparative study. *The Journal of neuroscience* 7: 2423–2432.
56. Amedee T, Robert A, Coles J (1997) Potassium homeostasis and glial energy metabolism. *Glia* : 599–630.
57. Furman CS, Gorelick-Feldman DA, Davidson KGV, Yasumura T, Neely JD, et al. (2003) Aquaporin-4 square array assembly: opposing actions of M1 and M23 isoforms. *Proceedings of the National Academy of Sciences of the United States of America* 100: 13609–13614.
58. Enger R, Gundersen GA, Haj-Yasein NN, Eilert-Olsen M, Thoren AE, et al. (2012) Molecular scaffolds underpinning macroglial polarization: an analysis of retinal Müller cells and brain astrocytes in mouse. *Glia* 60: 2018–2026.
59. Safronov BV, Wolff M, Vogel W (1999) Axonal expression of sodium channels in rat spinal neurones during postnatal development. *The Journal of Physiology* 514 (Pt 3): 729–734.
60. Louveau A, Smirnov I, Keyes TJ, Eccles JD, Rouhani SJ, et al. (2015) Structural and functional features of central nervous system lymphatic vessels. *Nature* 523: 337–341.
61. Iliff JJ, Wang M, Liao Y, Plogg BA, Peng W, et al. (2012) A Paravascular Pathway Facilitates CSF Flow Through the Brain Parenchyma and the Clearance of Interstitial Solutes, Including Amyloid β . *Science Translational Medicine* 4: 147ra111–147ra111.
62. Haj-Yasein NN, Bugge CE, Jensen V, Østby I, Ottersen OP, et al. (2015) Deletion of aquaporin-4 increases extracellular K(+) concentration during synaptic stimulation in mouse hippocampus. *Brain structure & function* 220: 2469–2474.
63. Zhang H, Verkman AS (2008) Aquaporin-4 independent Kir4.1 K+ channel function in brain glial cells. *Molecular and cellular neurosciences* 37: 1–10.
64. Amiry-Moghaddam M, Williamson A, Palomba M, Eid T, de Lanerolle NC, et al. (2003) Delayed K+ clearance associated with aquaporin-4 mislocalization: phenotypic defects in brains of alpha-syntrophin-null mice. *Proceedings of the National Academy of Sciences of the United States of America* 100: 13615–13620.
65. Tong J, Briggs MM, McIntosh TJ (2012) Water Permeability of Aquaporin-4 Channel Depends on Bilayer Composition, Thickness, and Elasticity. *Biophysical Journal* 103: 1899–1908.
66. Xie L, Kang H, Xu Q, Chen MJ, Liao Y, et al. (2013) Sleep Drives Metabolite Clearance from the Adult Brain. *Science* 342: 373–377.
67. Iliff JJ, Wang M, Zeppenfeld DM, Venkataraman A, Plog BA, et al. (2013) Cerebral arterial pulsation drives paravascular CSF-interstitial fluid exchange in the murine brain. *Journal of Neuroscience* 33: 18190–18199.

68. Hladky SB, Barrand MA (2014) Mechanisms of fluid movement into, through and out of the brain: evaluation of the evidence. *Fluids and Barriers of the CNS* 11: 26.
69. Smith AJ, Jin BJ, Verkman AS (2015) Muddying the water in brain edema? *Trends in neurosciences* 38: 331–332.
70. Thrane AS, Rangroo Thrane V, Plog BA, Nedergaard M (2015) Filtering the muddied waters of brain edema. *Trends in neurosciences* 38: 333–335.
71. Silberstein C (2004) Membrane organization and function of M1 and M23 isoforms of aquaporin-4 in epithelial cells. *AJP: Renal Physiology* 287: F501–F511.
72. Amiji MM, Sandmann BJ (2002) *Applied Physical Pharmacy*. McGraw-Hill.
73. Jung JS, Bhat RV, Preston GM, Guggino WB, Baraban JM, et al. (1994) Molecular characterization of an aquaporin cDNA from brain: candidate osmoreceptor and regulator of water balance. *Proceedings of the National Academy of Sciences of the United States of America* 91: 13052–13056.
74. Hashido M, Kidera A, Ikeguchi M (2007) Water transport in aquaporins: osmotic permeability matrix analysis of molecular dynamics simulations. *Biophysical Journal* 93: 373–385.
75. Bear MF, Paradiso MA, Connors BW (2001) *Neuroscience: Exploring the Brain*. Baltimore: Lippincott Williams and Wilkins, 2nd edition.
76. Hertz L, Peng L, Dienel GA (2006) Energy metabolism in astrocytes: high rate of oxidative metabolism and spatiotemporal dependence on glycolysis/glycogenolysis. *Journal of cerebral blood flow and metabolism : official journal of the International Society of Cerebral Blood Flow and Metabolism* 27: 219–249.
77. Goriely A, Geers MG, Holzapfel GA, Jayamohan J, Jrsalem A, et al. (2015) Mechanics of the brain: perspectives, challenges, and opportunities. *Biomechanics and Modeling in Mechanobiology* : 1–35.
78. Baber K, Mosthaf K, Flemisch B, Helmig R, Müthing S, et al. (2012) Numerical scheme for coupling two-phase compositional porous-media flow and one-phase compositional free flow. *IMA journal of applied mathematics* 77: 887–909.
79. Cattaneo L, Zunino P (2013) Computational models for coupling tissue perfusion and microcirculation. *MOX Report* 25/2013 .
80. Biot MA (1941) General theory of three-dimensional consolidation. *Journal of applied physics* 12: 155–164.
81. Bai M, Elsworth D, Roegiers JC (1993) Multiporosity/multipermeability approach to the simulation of naturally fractured reservoirs. *Water Resources Research* 29: 1621–1633.
82. Tully BJ, Ventikos Y (2011) Cerebral water transport using multiple-network poroelastic theory: application to normal pressure hydrocephalus. *Journal of Fluid Mechanics* 667: 188–215.
83. Vardakis JC, Tully BJ, Ventikos Y (2013) Exploring the efficacy of endoscopic ventriculostomy for hydrocephalus treatment via a multicompartamental poroelastic model of CSF transport: A computational perspective. *PloS ONE* 8: 1–16.
84. Rutkowska G, Haughton V, Linge S, Mardal KA (2012) Patient-specific 3d simulation of cyclic csf flow at the craniocervical region. *American Journal of Neuroradiology* 33: 1756–1762.
85. Støverud K, Langtangen H, Haughton V, Mardal K (2013) Csf pressure and velocity in obstructions of the subarachnoid spaces. *The neuroradiology journal* 26: 218–226.

86. Kandel ER, Markram H, Matthews PM, Yuste R, Koch C (2013) Neuroscience thinks big (and collaboratively). *Nat Rev Neurosci* 14: 659–664.
87. Einevoll G, Kayser C, Logothetis N, Panzeri S (2013) Modelling and analysis of local field potentials for studying the function of cortical circuits. *Nature Reviews Neuroscience* 14: 770–785.
88. Nunez PL, Srinivasan R (2006) *Electric fields of the brain: The Neurophysics of EEG*. Oxford University Press, Inc., 2nd ed. edition.
89. Hämäläinen M, Hari R, Ilmoniemi R, Knuutila J, Lounasmaa OV (1993) Magnetoencephalography - theory, instrumentation, and applications to noninvasive studies of the working human brain. *Reviews of Modern Physics* 65: 413–497.
90. Devor A, Boas D, Einevoll G, Buxton R, Dale A (2012) Neuronal basis of non-invasive functional imaging: from bold fmri to microscopic neurovascular dynamics. In: Choi IY, Gruetter R, editors, *Neural Metabolism In Vivo*, Springer. pp. 433-500.